Canadian Science Publishing | Canadian Geotechnical Journal

Discrete Element Modelling of Rock Creep Behaviour using Rate Process Theory

Journal:	*Canadian Geotechnical Journal*
Manuscript ID	cgj-2020-0124.R2
Manuscript Type:	Article
Date Submitted by the Author:	06-Oct-2020

Complete List of Authors:	Gutiérrez-Ch, José; Univ Politecnica Madrid Senent, Salvador; Univ Politecnica Madrid Estebanez, Eduardo; Univ Politecnica Madrid Jimenez, Rafael; Univ Politecnica Madrid

Keyword:	uniaxial compression, multistage creep test, creep strain, tertiary creep
Is the invited manuscript for consideration in a Special Issue? :	Not applicable (regular submission)

SCHOLARONE™ Manuscripts

DISCRETE ELEMENT MODELLING OF ROCK CREEP BEHAVIOUR USING RATE PROCESS THEORY

Gutiérrez-Ch J.G.*, Senent S.*, Estebanez E. and Jimenez R.*

*Universidad Politécnica de Madrid
C/Prof. Aranguren s/n, Madrid 28040, Spain
e-mail: jg.gutierrez@upm.es, s.senent@upm.es, rafael.jimenez@upm.es
Corresponding Author: R. Jimenez

ABSTRACT

Rock creep behavior is crucial in many rock engineering projects. Different approaches have been proposed to model rock creep behavior; however, many cannot reproduce tertiary creep (i.e., accelerating strain rates leading to rock failure). In this work, a discrete element model (DEM) is employed, in conjunction with the rate process theory [Kuhn MR, Mitchel JK. Modelling of soil creep with the discrete element method. *Eng Computations*. 1992;9(2):277–287] to simulate rock creep. The DEM numerical sample is built using a mixture of contact models between particles that combines the Flat Joint Contact Model and the Linear Model. Laboratory uniaxial compression creep tests conducted on intact slate samples are used as a benchmark to validate the methodology. Results demonstrate that, when properly calibrated, DEM models combined with the rate process theory can reproduce all creep stages observed in slate rock samples in the laboratory, including tertiary creep, without using constitutive models that incorporate an explicit dependence of strain rate with time. The DEM results also suggest that creep is associated with damage in the samples during the laboratory tests, due to new micro-cracks that appear when the load is applied and maintained constant at each loading stage.

Keywords uniaxial compression multistage creep test, DEM, rate process theory creep strain, tertiary creep.

1. Introduction

The time-dependent (creep) behaviour of rocks is an essential factor for many geotechnical projects, such as caverns and tunnels (Zhang et al. 2012; 2015), rock-bolts and rock anchors (Wyllie 1999) or rock-socketed piles (Tang et al. 1994); as well as for other topics such as underground storage of radioactive waste and geothermal energy (Dahhaoui et al. 2017) or mining and petroleum engineering applications (Hamza and Stace 2018).

Creep is a progressive and time dependent deformation associated with a plastic deformation that many geomaterials –e.g., soils, rocks, etc.– exhibit under a state of constant homogeneous stress (Brantut et al. 2012; 2013; Kuhn and Mitchel 1992). Such time-dependent behaviour can be studied through in-situ or laboratory creep tests; however, laboratory tests are often preferred because the range of temperature and pressure required to reproduce field conditions is easier to provide and control, so that their associated cost is often less than the cost of in-situ tests (Dusseault and Fordham 1993; Roy and Rao 2015). Although some standards to conduct creep tests in the laboratory have been proposed (see e.g., ISRM 2007; ASTM D7070-16 2016), the creep behaviour of rocks has been studied using different types of laboratory creep tests, such as oedometric compression (Mohajerani et al. 2011), direct shear (Larson and Wade 2001; Zhang et al. 2011), uniaxial compression (Yang et al. 1999), or triaxial compression (Zhang et al. 2012; 2015; Liu et al. 2018).

Laboratory creep tests reported in the literature have analyzed different rock types, such as fine-grained clastic rocks (Larson and Wade 2001; Mohajerani et al. 2011; Hamza and Stace 2018; Liu et al. 2018; Gent et al. 2018); sandstone (Brantut et al. 2014; Cao et al. 2014) and other clastic rocks (Zhang et al. 2013; 2015); slate (Min et al. 2014); salt rock (Li et al. 2018); or limestone (Cogan 1976; Maranini and Brignoli 1999; Brantut et al. 2014), shale (Cogan 1976), marble (Zhao et al. 2012), and granite (Kranz 1980; Fujii et al. 1999; He et al. 2016;) and other crystalline rocks (Damjanac and Fairhurst 2010). These investigations have emphasized on different aspects of creep behavior such as microstructure state, clay content, relative humidity, water content and chemistry of the pore fluid, temperature, deviatoric stress and effective pressure.

Many theoretical frameworks have been proposed to explain and interpret the creep behaviour of materials (see e.g., Dusseault and Fordham 1993). The Burger model, for instance, has been commonly employed to model rock creep (see Zhang et al. 2015; Hamza and Stace 2018); this model, however, cannot reproduce the accelerating strains associated to tertiary creep –a phase of creep behaviour in which strain rate increases rapidly and rock failure occurs, see Section 2– (Xu et al. 2013; He et al. 2016). This is also true for other models, for example based on the sliding wing crack (Ashby and Sammis 1990; Brantut et al. 2012). Methods to describe rate-dependent material failure, and to anticipate the onset of failure under creep conditions, have also been proposed (Voight 1989).

Kuhn and Mitchel (1992,1993) demonstrated that the rate process theory of Eyring (1936) –a theory that describes the sliding velocity between particles as a function of their tangential-to-normal force ratio, among other factors– could be employed to describe soil creep. For instance, the rate process theory has been shown to successfully explain, without an explicit dependence of strain rate on time, the dependence of creep strain on stress level and temperature; furthermore, intrinsically time-dependent mechanisms can be observed if an assembly of particles –like in a discrete element model– is considered (Kuhn and Mitchel 1992; Kwok and Bolton 2010).

Numerical methods –such as the Finite Element Method (FEM) or the Distinct Element Method (DEM)– have also gained recent attention to study the creep behaviour of rocks and rock masses (Kemeny 2005; Lisjak and Grasseli 2014). In particular, the DEM approach, in conjunction with the rate process theory, has been shown to be particularly useful to model soil creep (Kuhn and Mitchel 1992;1993; Kwok and Bolton 2010; Liu et al. 2019). Similarly, Li et al. (2017; 2018) have studied the creep of salt rocks employing the DEM and the Burger model. However, Kuhn and Mitchel's model has been developed and employed for sandy soils, and there is still an open research question regarding its applicability for rock materials subjected to creep.

In this work, the DEM and the rate process theory are employed to simulate rock creep. To that end, the results of laboratory uniaxial compression creep tests (on intact slate samples), that were available in the context of the construction project for a high speed railway tunnel (Ministerio de Fomento, 2012), are used as a benchmark to calibrate and validate the results of the numerical models developed in this work.

2. Fundamentals of creep modelling using rate process theory

An idealized creep behaviour consists of the following main phases (see **Fig. 1**): first, an almost instantaneous elastic strain occurs as a response to a rapid load increase, until a specified stress value is reached (A→B); then, if a sufficiently high stress is maintained, the following three stages could be noted: (i) the strain increases with a strain rate that decreases with time (primary creep, B→C); (ii) then, a stage with a quasi-constant strain rate follows (secondary creep C→D); and finally, (iii) the strain accelerates and rock failure occurs (tertiary creep, D→E) (Hamza and Stace 2018).

[Fig. 1 approx. here]

Kuhn and Mitchel (1992; 1993) proposed that creep strain occurs due to sliding between particles, so that the sliding velocity ($\dot{s}$) at each contact between particles depends on its tangential-to-normal force ratio (f^t/f^n) which can change during deformation even under constant boundary stresses (Mitchell and Soga 2005). The relationship between sliding velocity and tangential-to-normal force ratio can be modelled using the rate process theory proposed by Eyring (1936). The constitutive equation of rate process theory can be written as (Kuhn and Mitchel 1992):

$$\dot{s} = \lambda \frac{2kT}{h} e^{\frac{-\Delta F}{RT}} \sinh\left(\frac{1}{2kT} \frac{1}{n_1} \frac{f^t}{f^n}\right) \tag{1}$$

where λ is the flow unit, k is Boltzmann's constant ($1.381 \times 10^{-23}\,\mathrm{J\,K^{-1}}$), T is the absolute temperature (K), h is Planck's constant ($6.626 \times 10^{-34}\,\mathrm{J\,s}$), ΔF is the activation energy ($\mathrm{kJ\ mol^{-1}}$), R is the universal gas constant ($8.314 \times 10^{-3}\ \mathrm{kJ\ K^{-1}\ mol^{-1}}$), n_1 is the number of bonds per unit of normal contact force ($\mathrm{bonds/N}$), and f^t/f^n can be expressed as the friction coefficient at contacts between particles ($\mu = f^t/f^n$).

The main aspects of rate process theory that affect creep behaviour of a DEM model are (these explanations are mainly based on Mitchell and Soga 2005, where additional details can be found):

a) The activation energy (ΔF) represents the energy that a particle needs to slide with respect to another particle, so that both are in equilibrium. The activation energy controls the breakage of strong bonds and depends on the material: e.g., soils have an activation energy of about 40 to 400 $\mathrm{kJ/mol}$, metals of around 210 $\mathrm{kJ/mol}$, etc.
b) The flow unit (λ) is the separation distance between successive equilibrium positions in the interparticle contact structure, so that an amount of energy ΔF is needed to move the particles from one position to another. This movement, of magnitude equal to λ, could cause a single bond to break, or the simultaneous breakage of several bonds.
c) The number of bonds (n_1) at any contact depends on the compressive force transmitted at the contact –e.g., the number of bonds is directly proportional to the effective consolidation pressure for normally consolidated clays– so that the macroscopic strength is directly proportional to the number of bonds.

d) An increase in temperature (T) decreases the strength and the sliding velocity ($\dot{s}$) at each contact, so that (i) creep rates increase and (ii) the relaxation stresses corresponding to specific values of strain decrease.

e) The friction coefficient at contact particles ($\mu = f^t/f^n$) represents the "visco-frictional" nature of interparticle sliding (Eyring 1936). A decrease in the friction coefficient decreases the sliding velocity ($\dot{s}$) at every contact.

3. Fundamentals of DEM modelling with PFC

The Particle Flow Code (PFC) is the commercial code developed by Itasca Consulting Group Inc. (2014) used in this paper. PFC employs a distinct element modeling framework (Potyondy and Cundall 2004) to simulate the behaviour of different materials composed by a collection of rigid and finite-sized particles with a random distribution of sizes, and that can translate and rotate independently to each other. These particles interact at pair-wise contacts with internal forces and moments. Newton's second law, together with a force-displacement law, are employed to control the interactions between particles, to assess the contact forces, and to calculate particle displacements. In particular, the system evolution is computed using an explicit dynamic scheme –a time-stepping algorithm– to solve Newton's laws of motion (Itasca Consulting Group Inc. 2014).

To model the interactions between particles, PFC provides a Bonded-Particle Model (BPM) (Potyondy 2015) with several possible bond/contact models –e.g., Linear Model (LM), Linear Parallel Bond Model (LPBM), Flat-Joint Contact Model (FJCM), etc.– that can mimic the macroscopic behaviour of bonded materials (such as rock). In the BPM, the LM models the behaviour of an infinitesimal interface – which does not resist rotation– with linear and dashpot components (see **Fig. 2**a). The linear component simulates linear elastic frictional behaviour –non-tension springs with constant normal and shear stiffness–, while the dashpot reproduces viscous behaviour (Itasca Consulting Group Inc. 2014). On the other hand, the FJCM simulates the contact between particles using locally notional (bonded or unbonded) surfaces discretized into elements (see **Fig. 2**b) (Potyondy 2012). In FJCM, the behaviour of bonded interfaces is linear elastic until the bond strength is reached and the bond breaks, hence making the interface unbonded (Itasca Consulting Group Inc. 2014). Unbonded interfaces have a linear, elastic and frictional behaviour. In the LM and the FJCM, the slip is simulated by imposing a Coulomb limit on the shear force through the friction coefficient. For additional details, see Potyondy (2015) and Itasca Consulting Group Inc. (2014).

[Fig. 2 approx. here]

Following Li et al. (2017), we simulate rock creep behaviour using a DEM model with a mixture of different models of contact between particles; in particular, a mixture of LM and FJCM is employed, but with a significant preponderance of the FJCM with respect to the LM. FJCM is selected due to its ability to reproduce the behaviour of rock under direct tension and compression tests (Potyondy 2012); and, in particular, for its ability to reproduce the behaviour of intact rocks with a uniaxial compressive strength to tensile strength (σ_c/σ_t) ratio of more than 10 (Bahaaddini et al. 2019) –which is on the order of the σ_c/σ_t ratio reported by Ministerio de Fomento (2012) for rocks similar to those considered in this work–.

Note, however, that several LM contacts are necessary to model creep, as almost no creep occurs when they are removed from the DEM model (the selection of LM-to-FJCM contact ratio is based on a sensitivity analysis, see Section 5.2).

Different to the approach by Li et al. (2017) –who used the Burger and linear parallel bond models–, the rate process theory has been implemented into the DEM numerical model. To do that, Eq. (1) has been rewritten as:

$$\dot{s} = \alpha \sinh\left(\beta\mu\right) \tag{2}$$

Or approximately:

$$\dot{s} \approx \frac{\alpha}{2} e^{\beta\mu} \tag{3}$$

Where:

$$\alpha = \lambda \frac{2kT}{h} e^{\frac{-\Delta F}{RT}} \tag{4}$$

$$\beta = \frac{1 \;\; 1}{2kTn_1} \tag{5}$$

According to Kuhn and Mitchell (1992,1993) and using the parameters listed in **Table 1**, Eq. (3) can be simplified to Eq. (6) (see **Fig. 3**). Note that, since the main objective of this work is to validate the viability of the rate process theory to qualitatively simulate creep in rocks, the influence of rate process theory parameters are not studied; for a recent discussion on the influence of these parameters on the evolution of creep (in soils) see Liu et al. (2019).

$$\dot{s} \approx 2.727 \times 10^{-15} e^{37\mu} \tag{6}$$

[Table 1 approx. here]

[Fig. 3 approx. here]

Next, Eq. (6) has been implemented into the PFC model as a Visual C++ function that is compiled as a Dynamic Link Library (DLL) file, hence providing a 10-100-fold efficiency increase in relation to its implementation as a FISH function (Itasca Consulting Group Inc. 2014). (FISH is the internal programming language in PFC that enables the user to interact with PFC models, Itasca Consulting Group Inc. 2014). With this function, and at each time-stepping of the DEM simulation: (i) the sliding velocity ($\dot{s}$) at each ball-ball contact –i.e., the tangential component of their relative velocity– is computed; and (ii) the corresponding friction coefficient (μ) of the contact model –i.e., LM or FJCM– is modified using Eq. (6) and **Fig. 3**. For additional details about the DEM implementation of rate process theory, see Kuhn and Mitchell (1992,1993) and Kwok and Bolton (2010).

4. Laboratory tests

As comparison benchmark, we employ the results of compression creep tests conducted on intact slate samples available from Ministerio de Fomento (2012) (Note that, since tests were conducted by others, we will not discuss the experimental design in detail; rather, we will employ the available test results as a comparison benchmark of our numerical tool so that, given the existing experimental uncertainties, our goal is to reproduce the creep behaviour of soft rock in a qualitative way only). For completeness, however, a short description of the rock and tests analyzed is presented next.

The samples of natural slate used in this work were obtained from cylindrical cores from boreholes drilled in the Nogueira Group from the Galicia-Trás-Os-Montes Zone (north of Spain) during geotechnical investigations for Del Espino tunnel

(Ministerio de Fomento 2012). These are rocks of the Silurian Period, and samples were taken at depths ranging from 41.8 m to 93.9 m. The cylindrical samples to be tested were saw-cut to have a height-to-diameter ratio ($^{H}/_{D}$) of about 2.2, with $D = 62.1$ mm. To identify the mineralogical composition of the rock samples, optical microscopic tests were conducted. **Table 2** lists the mineral composition and its corresponding grain size of the two slate samples analyzed herein.

[Table 2 approx. here]

There are several ways to conduct compression creep tests in the laboratory (Dusseault and Fordham 1993; Maranini and Brignoli 1999): for instance, tests with steps of constant stress ($\sigma =$ constant), tests with constant strain rate ($\dot{\varepsilon} =$ constant), or relaxation or constant strain tests ($\varepsilon =$ constant). In this work, we employ experimental data from uniaxial compression multistage creep tests (UCMCTs). In these tests, stress levels are increased in steps (or stages), so that the associated strains were measured during the duration of each step. In particular, such UCMCTs were conducted at room temperature on two slate samples (Sample 1 and Sample 2). For each new loading step, the corresponding load increment was applied first, under a loading rate of about 0.35 MPa/s; then, the axial stress (σ_1) was kept constant for a specified time interval, during which the axial (ε_1) and the transverse (ε_3) strains were continuously monitored using two strain gauges with 2 cm length adhered to the rock sample at approximately one half of its height. The results of these laboratory tests will be presented in **Fig. 8** and **Fig. 9**, where the results of the numerical models will be also included. The physical time of the UCMCTs on Sample 1 and Sample 2 were 94 and 71 hours, respectively. Note also that the samples fail during different test stages: Sample 1 fails during one large load increment, whereas Sample 2 fails during creep associated to a constant stress. **Fig. 4** shows the evolution, for each loading step, of the elastic increments –i.e., without considering creep– of axial strain computed from the elastic portions of the stress-strain curve measured in the laboratory. The Young's modulus computed for such elastic portions of the stress-strain curves are almost constant for all the loading stages, except for the first ones, where the behavior of the samples is more rigid. (A possible interpretation for this behaviour is discussed below.)

[Fig. 4 approx. here]

5. Set-up of the numerical model to simulate rock creep tests in DEM

This work aims to reproduce the rock creep behaviour measured in the laboratory using two-dimensional DEM numerical models that implement the rate process theory. To that end, the DEM micromechanical parameters of the LM and of the FJCM are calibrated against the experimental data; i.e., against the results of the available uniaxial compression multistage creep tests (UCMCT). The procedure is discussed next.

5.1 Numerical uniaxial compression creep test

To conduct the numerical UCMCT, a numerical sample composed of cylindrical particles needs to be generated first. To that end, the procedure proposed by Potyondy and Cundall (2004) is used. Its steps are:

1) *Initial particle assembly*: a container of the same height as the sample (136.7 mm) and consisting of four planar frictionless walls is filled with an assembly of randomly placed particles. (For illustration, see **Fig. 5**a in which fewer particles are shown than those employed in the actual simulations: 3956 particles were employed in our simulations in Samples 1 and 2).

2) *Application of an isotropic initial stress:* to reduce the locked-in forces and to get a better distribution of contacts, the radii of all particles are iteratively changed, without still removing the boundary walls, until a specified isotropic stress ($\sigma_o^c \cong$ 1% of the uniaxial compressive strength) is reached. To do this, measurement circles (e.g., three circles) are installed inside the container and the isotropic stress ($\sigma_o = (\sigma_{11} + \sigma_{22})/2$) within each auxiliary circle is computed for each step (see **Fig. 5**b). The process finishes when the normalized difference ($(\sigma_o^c - \sigma_o)/\sigma_o^c$) is less than the isotropic stress tolerance (σ_{tol}); in agreement with previous works (Bahaaddini et al. 2014; Gutiérrez-Ch et al. 2018), $\sigma_{tol} = 0.5$ is used.

3) *Elimination of floating particles*: during the previous steps, "floating" particles with less than three contacts can appear (see **Fig. 5**c). At this step, the radii of floating particles are increased until all particles away from the specimen boundaries have at least three contacts.

4) *Application of the linear and flat-joint contact model*: linear and flat-joint contacts are installed depending on the gap between adjacent particles (g) and the given control gap value (g_c). In DEM models, g represents the

distance between balls at their contact, which could be (i) greater than zero or (ii) less than zero, or (iii) equal to zero, depending on the genesis of the DEM specimen (see **Fig. 6**). Therefore, the control gap (g_c) is a control distance employed to decide whether the LM or the FJCM are applied to that contact. The decision is made depending on the value of g resulting after the random generation of particles. To do that, a FISH function was used to check the particle-particle gap at each contact, and to assign to it the FJCM (if $g < g_c$) or LM (if $g \geq g_c$) (see **Fig. 5**d). Consequently, g_c allows us to calibrate the LM-to-FJCM contact ratio, as explained in Section 5.2. The micromechanical parameters of such linear and flat-joint contacts, as well as the LM-to-FJCM contact ratio of each model, are listed in **Table 3**. As indicated, there is a clear preponderance of FJCM with respect to the LM. This differentiates our analyses from previous works on soil creep using the rate process theory, in which only a cohesionless LM was employed (Kuhn and Mitchel 1993; Kwok and Bolton 2010).

5) *Remove the lateral walls*: the sample-genesis procedure is completed by (i) deleting the lateral (planar and frictionless) walls of the container and (ii) stepping the DEM algorithm until static equilibrium (see **Fig. 5**e).

Next, the following three steps (which were added in this work to reproduce the conditions of the sample in the laboratory) are applied to the generated sample:

6) *Initial stress:* the sample is loaded vertically up to an initial axial stress (σ_i) that could represent a valid initial situation of the laboratory tests after the upper platen is placed on the rock sample (see **Fig. 7**a). The initial stress

value has been calibrated so that, right after the application of the first loading stage of the test (step 7) (i.e. without considering any creep), the axial strain (ε_1) in the numerical model equals the axial strain in the laboratory test. Thereby, this value of axial strain serves as a reference for the rest of the test, allowing the comparison between numerical and laboratory results. Consequently, the axial and transverse strains (ε_1 and ε_3, respectively) obtained in this stage were neglected in subsequent analyses.

7) *Compression phase:* next, similar to Kwok and Bolton (2010), the numerical sample is loaded vertically at a constant strain rate $\dot{\varepsilon}_1$ of 5 %/s – i.e., a constant velocity of 0.003 m/s is applied at the top and bottom walls– until the sample reaches the axial stress (σ_1) of the first stage of the laboratory test (see **Fig. 7**b).

8) *Creep phase:* after the numerical sample has reached the specified axial stress (σ_1) corresponding to the first loading stage, the rock sample is allowed to creep while σ_1 is kept constant for a specified time interval. Such operation can be conducted employing the servo-control mechanism of PFC^{2D}, which allows one to control the translational velocity of selected walls, so that a desired force can be applied or maintained on them (see **Fig. 7**c). During this phase, the RPT is implemented using Eq. (6), which allows one to compute the friction coefficient associated with the sliding velocity ($\dot{s}$) between ball-ball contacts (for each time step). Then, such friction coefficient is applied to the model representing each corresponding

ball-ball contacts: i.e., the friction coefficient of the LM or FJCM applied to each ball-ball contact is modified at each time step.

At the first creep stage, and since the simulated time of the DEM test (t_{DEM}) is different from the physical time of the laboratory test (t_{lab}), their relationship can be calculated using the ε_1 reached after the first creep phase at the laboratory test as a benchmark. To that end, when the ε_1 reached at the first creep phase of the DEM test is equal to that obtained in the laboratory test, it is assumed that the corresponding t_{DEM} is equivalent to t_{lab}, and a time scaling relationship can be obtained (see **Table 3**). Such relationship (t_{DEM}/t_{lab}) allows us to compare results qualitatively (as done in Figs **9** and **10**) and to define the creep time in the DEM simulations of subsequent stages, as described next.

[Table 3 approx. here]

For multistage tests, such as the UCMCTs considered herein, steps 7 and 8 must be repeated until a maximum stress value (σ_{peak}) is reached and rock failure occurs. The creep time (t_{DEM}) in each loading stage –i.e., the time interval during which the axial stress is kept constant–, is calculated from the corresponding laboratory time (t_{lab}) interval using the t_{DEM}/t_{lab} scaling factor calculated in step 8.

During the UCMCT, the axial stress (σ_1) is obtained by dividing the average force reaction on the top and bottom walls by the sample cross-sectional area, while the axial and transverse strains (ε_1 and ε_3, respectively) are computed using a measurement circle (Itasca Consulting Group Inc. 2014) with a 2 cm diameter –i.e., equivalent to the length of the strain gauges employed during laboratory tests–

installed at the center of the sample (see **Fig. 7a**). (Note that the cross-section of the sample changes during the test and such change is considered to compute σ_1). Since the lateral walls needed to generate the sample are deleted, the change in the cross section of the sample is measured by tracking the displacement of two "gage particles": i.e., one particle at the right of the model and another at the left (see the blue balls in **Fig. 7**).

[Fig. 5 approx. here]

[Fig. 6 approx. here]

[Fig. 7 approx. here]

5.2 Calibration of micromechanical parameters of intact materials

Several procedures have been published in the literature to calibrate DEM micromechanical parameters, with results of the experimental uniaxial compression strength (UCS) tests being commonly used as benchmark (see e.g., Potyondy and Cundall 2004; Bahaaddini et al. 2014; Castro-Filgueira et al. 2017). This is probably because the UCS test of intact rocks can be estimated using relatively straightforward and cost-effective techniques, hence being one of the most commonly available and practical rock properties used in rock engineering (Shen et al. 2014). However, in this work, UCS tests are not available for the samples tested under creep, so that the calibration of the micromechanical parameters of the LM and the FJCM was conducted through a variation of the methodology proposed by Gutiérrez-Ch et al. (2018), in which the specific features of the UCMCT were considered.

The calibration procedure is iterative, and it starts by matching the macroscopic Young's modulus (E) of the linear (or elastic) portions of the strain-stress curves, which mainly depends on the effective modulus of the particles and of the flat-joints (E^* and $\overline{E^*}$); next, the cohesion (c) and tensile strength (σ_t) of the flat-joint are adjusted to reproduce the maximum stress value (σ_{peak}) reached at the UCMCT. In the latter adjustment, the friction angle (∅) is not considered, since a specific value of 30º, as proposed in the tunnel Project, is employed. (For more details about the calibration procedure, see Gutiérrez-Ch et al. 2018). The particle effective modulus (E^*_{LM}) and normal-to-shear stiffness ratio (k^*_{LM}) for the LM were the same as those employed for the FJCM. According to Kuhn and Mitchell (1992, 1993), and given that the rate process theory was incorporated into the PFC^{2D} numerical model, hence affecting the interactions between particles, no other damping –i.e., no other dashpot component– was required to be used in the LM. As indicated, the purpose of the present work is to analyses the use of DEM, in conjunction with the rate process theory, to simulate rock creep. Therefore, the influence of other parameters affecting a DEM model –e.g., particle size distribution, etc.–, are not considered. Note also that there might be different sets of micro-parameters that could reproduce a similar trend so that, it might be necessary to conduct a detailed study to optimize the calibration procedure, which is however out of the scope of this work.

Also, during the calibration procedure, a sensitivity analysis is conducted to select the LM-to-FJCM contact ratio to be employed. The first loading stage on Sample 1 –i.e., under a constant axial stress of 3.3 MPa– is employed to illustrate this, as shown in Figure 8. (To facilitate the visualization, since the laboratory test time is different to the simulation time used in DEM^{2D}, test times have been normalized with respect to their maximum values corresponding to the end of this loading stage). Results in **Fig 8** illustrate that an almost negligible creep strain occurs when a LM-to-FJCM contact ratio of 0% is used; therefore, LM-to-FJCM contact ratio must be increased to reproduce the creep behavior. Using a "trial and error" approach, a LM-to-FJCM contact ratio of 17.5 % is selected, as it is the one producing a better fit to the macroscopic rock creep behaviour of Sample 1 (see **Fig. 8**). **Table 1** lists the values employed for the rate process theory parameters. **Table 4** lists the micromechanical parameters obtained after the calibration, and **Table 5** compares the macroscopic UCMCTs results $-\sigma_{peak}, E-$ obtained in the laboratory for Samples 1 and 2 with those computed with DEM.

[Fig. 8 approx. here]

[Table 3 approx. here]

[Table 4 approx. here]

6. Results

6.1 Strain evolution during creep tests

Two (2) numerical uniaxial compression multistage creep tests (UCMCT) were conducted with DEM to simulate, with the procedure explained in Section 5.1, the creep behaviour on the slate rock described in Section 4.

Fig. 9a and **Fig. 10**a illustrate the stress "stages" employed during each UCMCT conducted in the laboratory. **Fig. 9**b and **Fig. 10**b compare (i) the evolutions of strain measured in the laboratory with (ii) the evolutions of strain computed with the calibrated DEM models that use the rate process theory. Since the laboratory test times (t_{lab}) are different from the simulated times (t_{DEM}) in DEM, t_{DEM} axes have been scaled, according to the t_{DEM}/t_{lab} factors (see Section 5.1), to allow a qualitative comparison between DEM and laboratory results. The DEM results, except for the first 2-3 loading steps, are quite similar to the laboratory results, hence suggesting that DEM models based on rate process theory, when properly calibrated, can be an adequate tool to model the creep behaviour of slate rocks. Furthermore, the results obtained from DEM are consistent with the results reported by Zhang et al. (2011), in which a fluctuating behavior is not present, demonstrating that creep strain in the numerical simulation is continuous over time.

The main differences between the DEM models and the laboratory tests occur during the initial loading steps –when creep is still not a main aspect controlling the strain behaviour of the samples–. This is expected, considering (i) the variation of the sample stiffness during the loading stages shown in **Fig. 4**, and (ii) that each DEM model has been calibrated employing a constant Young's modulus. Although the reason for this behavior in the laboratory tests is not completely clear, we argue that this is probably because the vertical strain field in the sample is still not homogenous during the initial test stages (due, for instance, to end effects).

[Fig. 9 approx. here]

[Fig. 10 approx. here]

Importantly (since many creep models cannot reproduce tertiary creep), **Fig. 9** and **Fig. 10** also show that DEM models based on rate process theory are suitable to simulate all stages (i.e., including tertiary creep) of a theoretical creep curve, such as that presented in **Fig. 1**. For the lower axial stresses (σ_1) associated with the initial loading stages, note (i) that only an "instantaneous" elastic strain and the initial phases of creep –i.e., primary and secondary creep– are observed, and (ii) that such creep strains are still minor during the initial loading stages. As an example, the detail in **Fig. 9** (corresponding to the $\sigma_1 = 16.5$ MPa step) illustrates the separation between primary creep (with diminishing rates of strains) and secondary creep (with constant strain rate). Similarly, the DEM model can reproduce the tertiary creep of the samples. This is more clearly illustrated on Sample 2, as this sample fails during the creep phase associated with the last loading steps of $\sigma_1 = 31.35$ MPa. (As indicated, Sample 1 fails during the load increment, so that tertiary creep is not observed). Again, these numerical results suggest that rate process theory and DEM are able to reproduce both types of failure without any user-defined intervention: i.e., to reproduce failure during a load increment; or to reproduce failure under tertiary creep for a constant load. (These results are in line with those obtained for soils by Kuhn and Mitchell 1992; 1993; Kwok and Bolton 2010; and Liu et al. 2019).

Fig. 9 and **Fig. 10** evidence that creep is more relevant on Sample 2 than on Sample 1. This could be due to its mineralogical composition (see **Table 2**), as clay minerals are mostly responsible for the strength reduction and the large strains associated to creep under constant load (Liu et al. 2018).

Fig. 11 shows the evolution of axial strain with axial stress (corresponding to the stages of constant σ_1) during DEM computations and during the laboratory tests: note that creep is negligible during the first axial loading steps –i.e., for $\sigma_1 \leq 9.9$ MPa on Sample 1 and $\sigma_1 \leq 6.6$ MPa on Sample 2–, whereas creep is clearly noticeable for subsequent loading stages, in which plastic strains also occur. Additionally, results show that creep rate increases when the axial stress increases, until the maximum stress (σ_{peak}) is reached and the rock sample fails.

[Fig. 11 approx. here]

6.2 Creep strain rate behaviour

Fig. 12a and **Fig. 13**a show the logarithm of axial strain rate ($\dot{\varepsilon}_1$) against the DEM time (t_{DEM}) during the UCMCTs conducted on Samples 1 and 2. (They also show when each new loading stage is applied). As additional load is applied in each loading stage, the axial strain rate increases quickly up to approximately $\dot{\varepsilon}_1$ of 5 %/s (similar to that applied by the walls), until the axial stress specified for such stage is reached; then the axial strain rate decreases gradually during primary creep, until it reaches a quasi-constant value (secondary creep). The strain behaviour for higher axial stress is similar to the behaviour for lower axial stress; however, the strain rate at the end of each stage tends to increase for higher load stages, even when their duration is equal to, or slightly shorter, than the duration of earlier stages with lower axial loads. This axial strain rate behaviour qualitatively agrees with the creep tests results conducted by Brantut et al. (2014, 2014) in porous limestone and sandstone.

Fig. 12b and **Fig. 13**b plot the logarithm of axial strain rate ($\dot{\varepsilon}_1$) against the logarithm of the DEM time (t_{DEM}), showing again that DEM results agree with the idealized creep behaviour in **Fig. 1**: A quasi-linear decrease of strain rate with the logarithm of time (primary creep) occurs at the beginning of each loading step, followed by another period of approximately constant strain rate (secondary creep). This occurs, with a different relative relevance of both phenomena, in all loading steps, except for the last loading step of (higher) stress in Sample 2, in which tertiary creep with accelerating strains occurs, leading to rock failure.

[Fig. 12 approx. here]

[Fig. 13 approx. here]

6.3 Creep failure behaviour

Fig. 14 and **Fig. 15** show the number of micro-cracks –produced in both shear and tension– and the progressive failure developed during the DEM numerical modeling of the UCMCTs tests conducted with Samples 1 and 2. As it can be observed, the number of such micro-cracks is very small for the loading stages corresponding to lower stress values; however, the number of tension cracks increases rapidly with the stress applied in each loading stage, as well as with the duration of such stage. In particular, a large increase of the number of micro-cracks occurs (i) immediately after application of the new load and (ii) during the creep stage.

Note also that numerical results suggest that the main failure mechanism on Samples 1 and 2 is caused by long-term damage induced by accumulation of micro-cracks during creep, hence reducing the strength of the rock sample with time, so that its failure is not sudden and is “delayed” in time, particularly in Sample 2.

Finally, it was found that rock failure occurs when a few shear micro-cracks are developed; this seems to coincide with an even faster rate of increase of the number of tension cracks within the sample when failure is approached (see **Fig. 14**). These results are consistent with those of Zhao et al. (2012) who, based on laboratory UCMCTs on sandstone, reported that creep failure of sandstone samples occurred when micro-fissures inside the samples reached a critical value producing an accelerating creep until failure. Also, this behaviour was observed by Baud and Meredith (1997), who studied creep in Darley Dale sandstone.

[Fig. 14 approx. here]

[Fig. 15 approx. here]

7. Conclusions

Rock creep behaviour is a crucial aspect in many rock engineering applications. Although many models have been proposed to reproduce rock creep, many of the most common ones cannot reproduce all phases of creep and, in particular, they cannot reproduce the accelerating strain rates associated to tertiary creep and leading to rock failure.

This work demonstrates that the discrete element method (DEM) can be employed, in conjunction with the rate process theory, to reproduce the creep behavior of slate rock samples from the Nogueira Group in Northern Spain, when they are subjected to uniaxial compression multistage creep tests (UCMCTs) conducted in the laboratory. To do that, and differentiating our approach to previous works that model soil creep (Kuhn and Mitchel 1992; 1993; Kwok and Bolton 2010; Liu et al. 2019), the DEM sample is constructed using a hybrid mixture of contact models between particles, employing both the Flat Joint Contact Model and the Linear Model, but with a significant preponderance of FJCM with respect to the LM. Note, however, that LM contacts are necessary to model creep, as almost no creep occurs when they are removed from the DEM model.

One significant novelty of the proposed approach with respect to other traditional approaches to model rock creep (such as, e.g., Burger's model) is that it can reproduce tertiary creep without having to resort to a constitutive model that explicitly characterizes tertiary creep; at the same time, it can reproduce failure of the sample during a load increment. (This is also the first time that rate process theory is used to simulate rock creep behavior, which required us to implement it into new rock specific DEM models). In particular, the rate process theory provides a fundamental micromechanical relationship between the sliding velocity between particles and their coefficient of friction; and it is shown that such fundamental relationship is able to model all stages of creep at the macroscopic level. Results also show that our DEM approach can reproduce the evolution of strain with time measured in real rock samples, including samples that failed after a tertiary creep stage.

The DEM models based on rate process theory proposed herein also provide interesting information about the evolution of damage during the creep tests conducted, suggesting that rock damage during such creep tests mainly occurs due to tensile fractures that develop during loading and during creep; the rate of tensile cracking is also very high during tertiary creep, when some shear cracks develop as well.

Finally, the model can be calibrated, in a relatively straightforward way, with the methodology provided, that uses information from the laboratory UCMCTs. Together with its capability to consider aspects such as the stresses or times associated to loading stages, etc.; this easy calibration makes this approach to become a cost and time-effective alternative to other in-situ tests that could be proposed to analyze rock creep behaviour. However, it may be more difficult to incorporate into the DEM models the influence of other factors, such as the mineralogical compositions of rock, and additional laboratory tests might be required. The influence of mineralogy on creep behaviour, however, is considered outside the scope of this research and it will be discussed in future publications.

8. Acknowledgements

This research was funded by the Spanish Ministry of Economy, Industry and Competitiveness under Project BIA 2015-69152-R. The first author was the recipient during 2019 of one Fellowship for PhD research provided by the José Entrecanales Ibarra Foundation. The support of both institutions is gratefully acknowledged.

9. References

Ashby, M.F., and Sammis, C.G. 1990. The damage mechanics of brittle solids in compression. Pure and Applied Geophysics, **133**(3): 489–521. doi:10.1007/BF00878002.

ASTM D7070-16. 2016. Standard test methods for creep of rock core under constant stress and temperature. doi:10.1520/D7070-16.

Bahaaddini, M., Hagan, P.C., Mitra, R., and Hebblewhite, B.K. 2014. Scale effect on the shear behaviour of rock joints based on a numerical study. Engineering Geology, **181**: 212–223. doi:10.1016/j.enggeo.2014.07.018.

Bahaaddini, M., Mohammad, A., and Masouri, H. 2019 Flat-joint model to reproduce the mechanical behaviour of intact rocks. European Journal of Environmental and Civil Engineering, 1–23. doi:10.1080/19648189.2019.1579759.

Baud, P., and Meredith, P.G. 1997. Damage accumulation during triaxial creep of darley dale sandstone from pore volumometry and acoustic emission. International Journal of Rock Mechanics and Mining Sciences, **34**(3–4): 24.e1–24.e10. doi:10.1016/S1365-1609(97)00060-9.

Brantut, N., Baud, P., Heap, M.J., and Meredith, P.G. 2012. Micromechanis of brittle creep in rocks. Journal of Geophysical Research: Solid Earth,**117**(B8): B08412. doi:10.1029/2012JB009299.

Brantut, N., Heap, M.J., Baud, P., and Meredith, P.G. 2014. Mechanism of time-dependent deformation in porous limestone. Journal of Geophysical Research: Solid Earth, **119**(7): 5444–5463. doi:10.1002/2014JB011186.

Brantut, N., Heap, M.J., Baud, P., and Meredith, P.G. 2014. Rate- and strain-dependent brittle deformation of rocks. Journal of Geophysical Research: Solid Earth, **119**(3):1818–1836. doi:10.1002/2013JB010448.

Brantut, N., Heap, M.J., Meredith, P.G., and Baud, P. 2013. Time-dependent cracking and brittle in crustal rocks: a review. Journal of Structural Geology, **52**:17–43. doi:10.1016/j.jsg.2013.03.007.

Cao, Y., Den, J., Yu, B., Tan, Q., and Ma, C. 2014. Analysis of sandstone creep and wellbore instability prevention. Journal of Natural Gas Science and Engineering, **19**: 237–243. doi:10.1016/j.jngse.2014.05.013.

Castro-Filgueira, U., Alejano, L., Arzúa, J., and Ivars, D.M. 2017. Sensitivity analysis of the micro-parameters used in a PFC analysis towards the mechanical properties of rocks. Procedia Engineering, **191**: 488–495. doi:10.1016/j.proeng.2017.05.208.

Cogan, J. 1976. Triaxial creep tests of Opohonga limestone and Ophir shale. International Journal of Rock Mechanics and Mining Sciences & Geomechanics Abstracts, **13**(1): 1–10. doi: 0.1016/0148-9062(76)90221-7.

Dahhaoui, H., Belayachi, N., and Zadjaoui, A. 2017. Modeling of creep behavior of an argillaceous rock by numerical homogenization method. Periodica Polytechnica Civil Engineering, **62**(2): 462–469. doi:10.3311/PPci.11697.

Damjanac, B., and Fairhurst, C. 2010. Evidence for a long-term strength threshold in crystalline rock. Rock Mechanics and Rock Engineering, **43**(5):513–531. doi:10.1007/s00603-010-0090-9.

Dusseault, M.B., and Fordham, C.J. 1993. Time-dependent behavior of rocks. Rock testing and site characterization: Principles Practice and Projects, 119–149. doi:10.1016/B978-0-08-042066-0.50013-6.

Eyring, H. 1936. Viscosity, plasticity and diffusion as examples of absolute reaction rates. The Journal of Chemical Physics, **4**(4): 283–291. doi:10.1063/1.1749836.

Fujii, Y., Kiyama, T., Ishijima, Y., and Kodama, J. 1999. Circumferential strain behavior during creep tests of brittle rocks. International Journal of Rock Mechanics and Mining Sciences, **36**(3): 323–337. doi:10.1016/S0148-9062(99)00024-8.

Geng, Z., Bonnelye, A., Chen, M., Jin, Y., Dick, P., David, C., Fang, X., and Shubnel, A. 2018. Time and temperature dependent creep in Tournemire shale. Journal of Geophysical Research: Solid Earth, **123**(11): 9658–9675. doi:10.1029/2018JB016169.

Gutiérrez-Ch, J.G., Senent, S., Melentijevic, S., and Jimenez, R. 2018. Distinct element method simulations of rock-concrete interfaces under different boundary conditions. Engineering Geology, **240**(5): 123–139. doi:10.1016/j.enggeo.2018.04.017.

Hamza, O., and Stace, R. 2018. Creep properties of intact and fractured muddy siltstone. International Journal of Rock Mechanics and Mining Sciences, **106**: 109–116. doi:10.1016/j.ijrmms.2018.03.006.

He, Z., Zhu, Z., Wu, N., Wang, Z., and Cheng, S. 2016. Study on time-dependent behavior of granite and the creep model based on fractional derivative approach considering temperature. Mathematical Problems in Engineering. 1–10. doi:0.1155/2016/8572040.

ISRM. 2007. The complete ISRM suggested methods for rock characterization, testing and monitoring: 1974–2006. In: Ulusay, R., Hudson, J.A., (eds) Suggested methods prepared by the commission on testing methods, international society for rock mechanics, compilation arranged by the ISRM Turkish National Group, Ankara, Turkey.

Itasca Consulting Group Inc. 2014. PFC^{2D} Manual, Version 5.0. (Minnneapolis, Minnesota).

Kemeny, J. 2005. Time-dependent drift degradation due to the progressive failure of rock bridges along discontinuities. International Journal of Rock Mechanics and Mining Sciences, **42**(1): 35–46. doi:10.1016/j.ijrmms.2004.07.001.

Kranz, R.L. 1980. The effects of confining pressure and stress difference on static fatigue of granite. Journal of Geophysical Research: Solid Earth, **85**(B4): 1854–1866. doi:10.1029/JB085iB04p01854.

Kuhn, M.R., and Mitchel, J.K. 1992. Modelling of soil creep with the discrete element method. Engineering Computations, **9**(2): 277–287. doi:10.1108/eb023866.

Kuhn, M.R., and Mitchel, J.K. 1993. New perspectives on soil creep. Journal of Geotechnical Engineering, **119**(3): 507–524. doi:10.1061/(ASCE)0733-9410(1993)119:3(507).

Kwok, C.Y., and Bolton, M.D. 2010. DEM simulations of thermally activated creep in soils. Géotechnique, **60**(6): 425–433. doi:10.1680/geot.2010.60.6.425.

Larson, M.K., and Wade, R.G. 2001. Creep along weak planes in roof and how it affects stability. Transactions of Society for Mining, Metallurgy, and Exploration, **310**:47–54.

Li, W., Han, Y., Wang, T., and Ma, J. 2017. DEM micromechanical modeling and laboratory experiment on creep behavior of salt rock. Journal of Natural Gas Science and Engineering, **46**: 38–46. doi:10.1016/j.jngse.2017.07.013.

Li, W., Zhu, C., Yang, C., Duan, K., and Hu, W. 2018. Experimental and DEM investigations of temperature effect on pure and interbedded rock salt. Journal of Natural Gas Science and Engineering, **56**: 29–41. doi:10.1016/j.jngse.2018.05.020.

Lisjak, A., and Grasselli, G. 2014. A review of discrete modeling techniques for fracturing processes in discontinuous rock masses. Journal of Rock Mechanics and Geotechnical Engineering, **6**(4): 301–314. doi:10.1016/j.jrmge.2013.12.007.

Liu, Z., Shao, J., Xie, S., Conil, N., and Zha, W. 2018. Effects of relative humidity and mineral compositions on creep deformation and failure of a claystone under compression. International Journal of Rock Mechanics and Mining Sciences, **103**: 68–176. doi:10.1016/j.ijrmms.2018.01.015.

Liu, S., Wang, J., and Kwok, C.Y. 2019. DEM simulation of creep in one-dimensional compression of crushable sand. J Journal of Geotechnical and Geoenvironmental Engineering, **145**(10): 04019060. doi:10.1061/(ASCE)GT.1943-5606.0002098.

Maranini, E., and Brignoli, M. 1999. Creep behaviour of a weak rock: experimental characterization. International Journal of Rock Mechanics and Mining Sciences, **36**: 127–138. doi:10.1016/S0148-9062(98)00171-5.

Min, H., LI, W., and Luxia, S. 2014. Experimental study on the creep mechanical properties of carbonaceous slate. Electronic Journal of Geotechnical Engineering,**19**: 6213–6230.

Ministerio de Fomento. 2012. “Proyecto de Construcción de Plataforma. Corredor Norte-Noroeste de Alta Velocidad. Línea de Alta Velocidad Madrid-Galicia. Tramo: Túnel del Espiño. Vía izquierda.” Anejo Nº 6, Madrid, Spain.

Mitchell, J.K., and Soga, K. 2005. Fundamentals of soil behaviour. 3er edn. New York: John Wiley.

Mohajerani, M., Delage, P., Monfared, M., Tang, A.M., Sulem, J., and Gatmiri, B. 2011. Oedometric compression and swelling behaviour of the Callovo-Oxfordian argillite. International Journal of Rock Mechanics and Mining Sciences, **48**(4): 605–615. doi:10.1016/j.ijrmms.2011.02.016.

Mufundirwa, A., Fujii, Y., and Kodama, J. 2010. A new practical method for prediction of geomechanical failure-time. International Journal of Rock Mechanics and Mining Sciences, **47**(7): 1079–1090. doi:10.1016/j.ijrmms.2010.07.001.

Potyondy, D.O., and Cundall, P.A. 2004. A bonded-particle model for rock. International Journal of Rock Mechanics and Mining Sciences, **41**(8): 1329–1364. doi:10.1016/j.ijrmms.2004.09.011.

Potyondy, D.O. 2012. A flat-jointed bonded-particle material for hard rock. In: 46th US Rock Mechanics/Geomechanics Symposium. Chicago, Illinois.

Potyondy, D.O. 2015. The bonded-particle model as a tool for rock mechanics research and application: current trends and future directions. Geosystem Engineering, **18**(1):1–28. doi:10.1080/12269328.2014.998346.

Roy, G.M., and Rao, K.S. 2015. Analysis of creep behaviour of soft rocks in tunneling. In: International Conference on “Engineering Geology in New Millennium”. New Delhi, India.

Shen, J., Jimenez, R., Karakus, M., and Xu, C. 2013. A simplified failure criterion for intact rocks based on rock type and uniaxial compressive strength. Rock

Mechanics and Rock Engineering, **47**(2): 357–369. doi:10.1007/s00603-013-0408-5.

Tang, Q., Drumm, E.C., and Bennett, R.M. 1994. Response of drilled shaft foundations in karst during construction loading. Proc. Int. Conf. Design and Construction of Deep Foundations, US Federal Highway Administration, Orlando, FL, 1296–1309.

Voight, B. 2003. A relation to describe rate-dependent material failure. Science, **243**(4888): 200-203. doi: 10.1126/science.243.4888.200.

Wyllie, D.1999. Foundations on rock. London: CRC Press.

Xu, T., Xu, Q., Tang, C., and Ranjith P.G. 2013. The evolution of rock failure with discontinuities due to shear creep. Acta Geotechnica, **8**(6): 567–581. doi:10.1007/s11440-013-0244-5.

Yang, C., Daemen, J.J.K., and Ying, J.H. 1999. Experimental investigation of creep behavior of salt rock. International Journal of Rock Mechanics and Mining Sciences, **36**(2): 233–242. doi:10.1016/S0148-9062(98)00187-9.

Zhang, Q., Shen, M., and Zhi, W. 2011. Investigation of mechanical behavior of a rock plane using rheological tests. Journal of Materials in Civil Engineering, **23**(8): 1220–1226. doi: 10.1061/(ASCE)MT.1943-5533.0000269.

Zhang, Y., Xu, W.Y., Gu, J.J., and Wang, W. 2013. Triaxial creep tests of weak sandstone from fracture zone of high dam foundation. Journal of Central South University, **20**(9): 2528–2536. doi:10.1007/s11771-013-1765-7.

Zhang, Y., Xu, W.Y., Shao, J.F., Zhao, H.B., and Wang, W. 2015. Experimental investigation of creep behaviour of clastic rock in Xiangjiaba Hydropower Project. Water Science and Engineering, **8**(1): 55–62. doi:10.1016/j.wse.2015.01.005.

Zhang, Z.L., Xu, W.Y., and Wang, W. 2012. Triaxial creep tests of rock from the compressive zone of dam foundation in Xiang-jiaba Hydropower Station. International Journal of Rock Mechanics and Mining Sciences, **50**(1):133–139. doi:10.1016/j.ijrmms.2012.01.003.

Zhao, X., Che,n B., Zhao, H., Jie, B., and Ning, Z. 2012. Laboratory creep tests for time-dependent properties of a marble in Jinping II hydropower station. Journal of Rock Mechanics and Geotechnical Engineering, **4**(2): 168–176. doi:10.3724/SP.J.1235.2012.00168.

List of Tables

Table 1. Constants employed for the rate process theory (according to Kuhn and Mitchell, 1993).

Variable	Value
Boltzmann's constant, k (J/K)	1.381×10^{-23}
Planck's constant, h (J.s)	6.626×10^{-34}
Universal gas constant, R (kJ/(mol.K)	8.314×10^{-3}
Absolute temperature, T (K)	293
Flow unit, λ (m)	3×10^{-10}*
Activation energy, ΔF (kJ/mol)	100*
Number of bonds per unit of normal contact force, n_1 (bonds/N)	1×10^{9}

*chosen to reproduce the experimental behavior within the range suggested by Kuhn and Mitchell (1993)

Table 2. Estimated mineral composition of the rock samples, based on optical microscopy tests.

	Sample 1		Sample 2	
	Minerals composition (%)	Grain size (mm)	Minerals composition (%)	Grain size (mm)
Quartz	19	0.008 – 0.016	20	0.008 – 0.016
Sericite	26	0.002	39	0.002
Opaque	50.5	-	31	-
Chlorite	4	0.04 – 0.16	3	0.03 – 0.12
Calcite	0.5	0.15	-	-
Others	-	-	1	-
Depth range (m)	92.7 – 93.3		43.6 – 44.2	

Table 3. Scale factor (t_{DEM}/t_{lab}) between the laboratory and DEM model.

Sample		Axial strain, ε_1 (%)	Time, t (s)	t_{DEM}/t_{lab}
1	Lab	3.6×10^{-3}	43120	1.16×10^{-6}
	DEM		0.050	
2	Lab	8.3×10^{-4}	2967.7	3.14×10^{-6}
	DEM		0.009	

Table 4. Micro-mechanical parameters fitted for the DEM employed to reproduce the UCMCTs conducted on slate rocks.

Sample	Particle micromechanical properties		FJCM micromechanical properties		Hybrid model	
1	E^* (GPa)	34.15	$\overline{E}^*$ (GPa)	34.15		
	$k^* = k_n/k_s$	1.80	$\overline{k}^*$	1.80	FJCM contacts	9069
	Friction angle $\emptyset$ (°)	30	c (MPa)	49.48		
	Ball density, $\rho (kg/m^3)$	2737	σ_t (MPa)	26.85	LM contacts	1588
	Minimum radius, R_{min} (mm)	0.60	FJ bonding ratio, c/σ_t	1.84		
	R_{max}/R_{min}	1.50	Bonded fraction, ϕ_B	1.00	LM-to-FJCM contact ratio (%)	17.5
			Gapped fraction, ϕ_G	0.00		
			Initial gap, g_o (mm)	0.05	Control gap, g_c (mm)	$-3.085x10^{-2}$
			Number of elements, N_r	2		
			LM micromechanical properties			
			E^*_{LM} (GPa)	34.15		
			k^*_{LM}	1.80		
2	E^* (GPa)	24.30	$\overline{E}^*$ (GPa)	24.30		
	$k^* = k_n/k_s$	1.80	$\overline{k}^*$	2.70	FJCM contacts	9070
	Friction angle $\emptyset$ (°)	30	c (MPa)	45.00		
	Ball density, $\rho (kg/m^3)$	2647	σ_t (MPa)	27.52	LM contacts	1587
	Minimum radius, R_{min} (mm)	0.60	FJ bonding ratio, c/σ_t	1.63		
	R_{max}/R_{min}	1.50	Bonded fraction, ϕ_B	1.00	LM-to-FJCM contact ratio (%)	17.5
			Gapped fraction, ϕ_G	0.00		
			Initial gap, g_o (mm)	0.05	Control gap, g_c (mm)	$-3.075x10^{-2}$
			Number of elements, N_r	2		
			LM micromechanical properties			
			E^*_{LM} (GPa)	24.3		
			k^*_{LM}	1.80		

Table 5. Comparison between macro-mechanical properties obtained for the UCMCTs conducted on slate rock samples, by laboratory tests and by DEM numerical tests.

Sample	Macro-properties	Lab	DEM
1	σ_{peak} (MPa)	36.30	36.10
	E (GPa)	37.23	37.19
2	σ_{peak} (MPa)	31.35	31.35
	E (GPa)	26.54	26.44

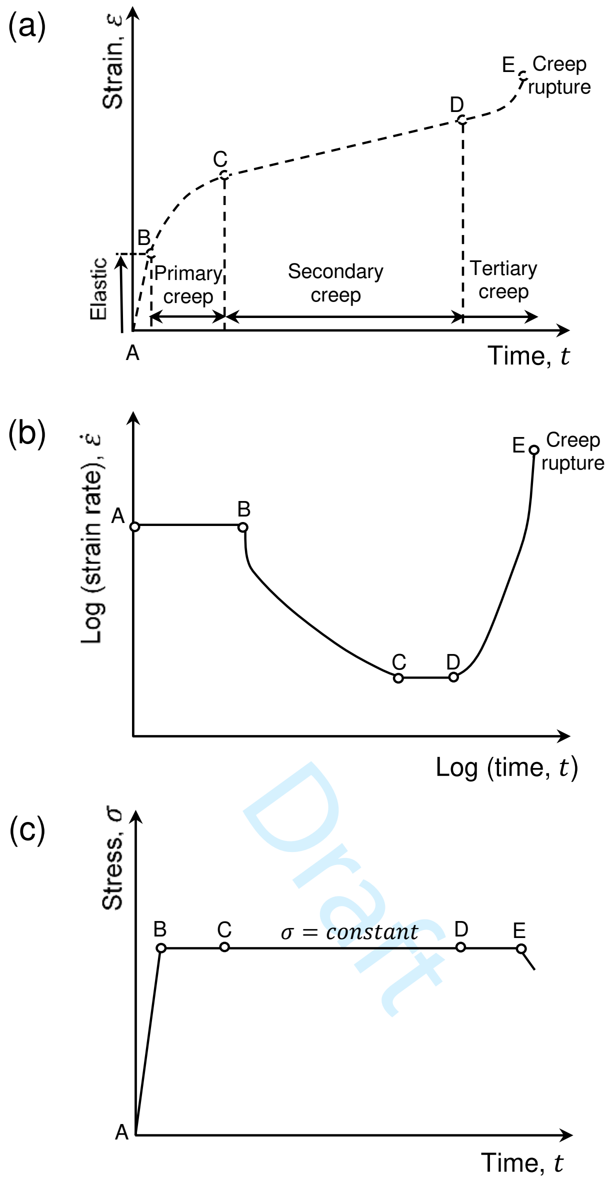

Fig. 1. Stages of creep under constant homogeneous stress: (a) strain versus time, (b) log(strain rate) versus log(time), (c) stress versus time (modified from Kwok et al. 2010)

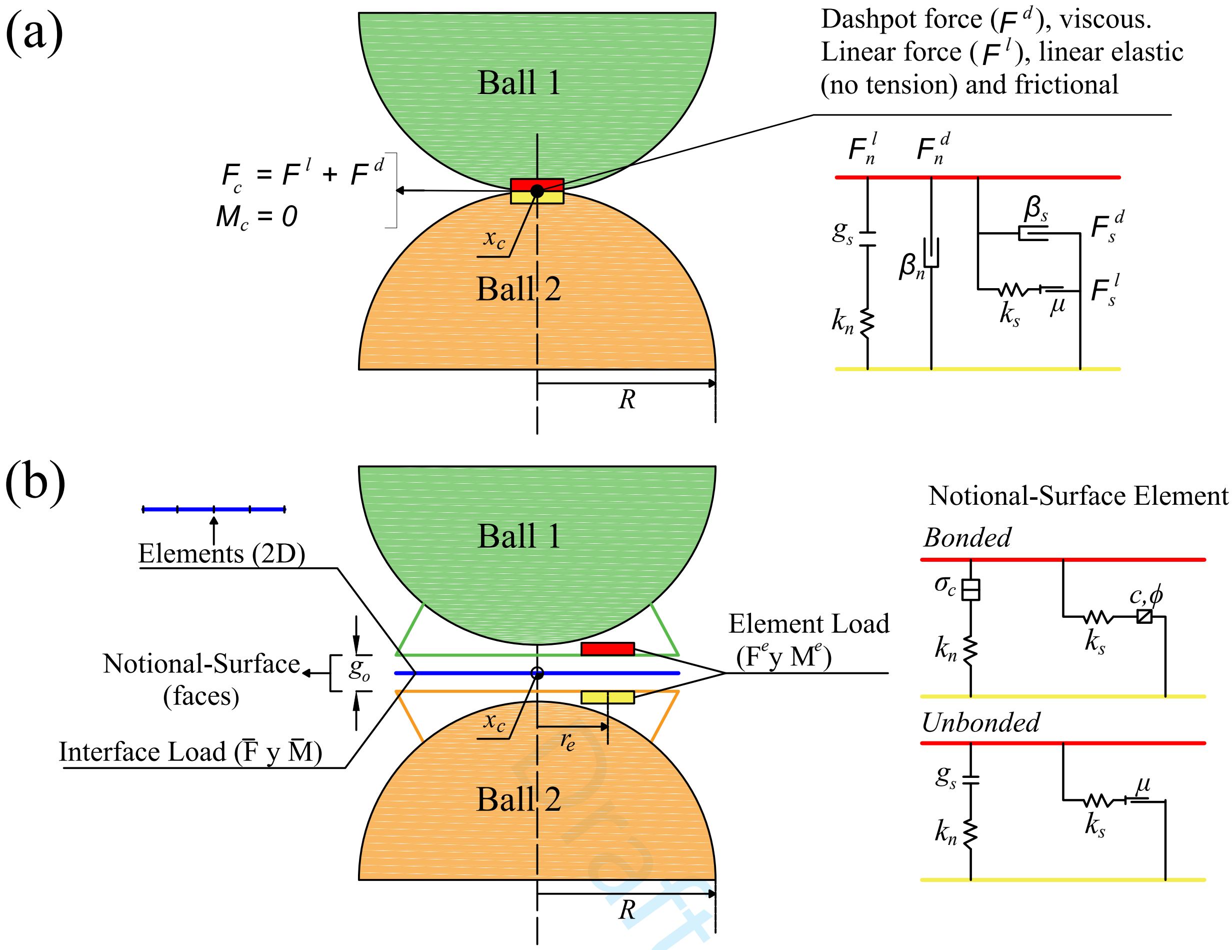

Fig. 2. Behavior and rheological components of the: (a) Linear Model (LM), (b) Flat Joint Contact Model (FJCM) (modified from Itasca Consulting Group Inc. 2014).

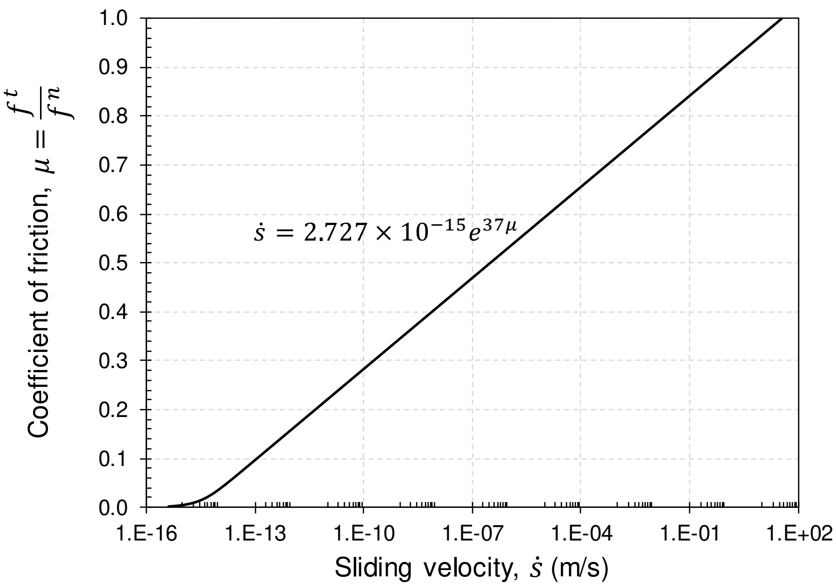

Fig. 3. Function of rate process theory employed in this work, providing a relationship between sliding velocity between particles and their corresponding coefficient of friction.

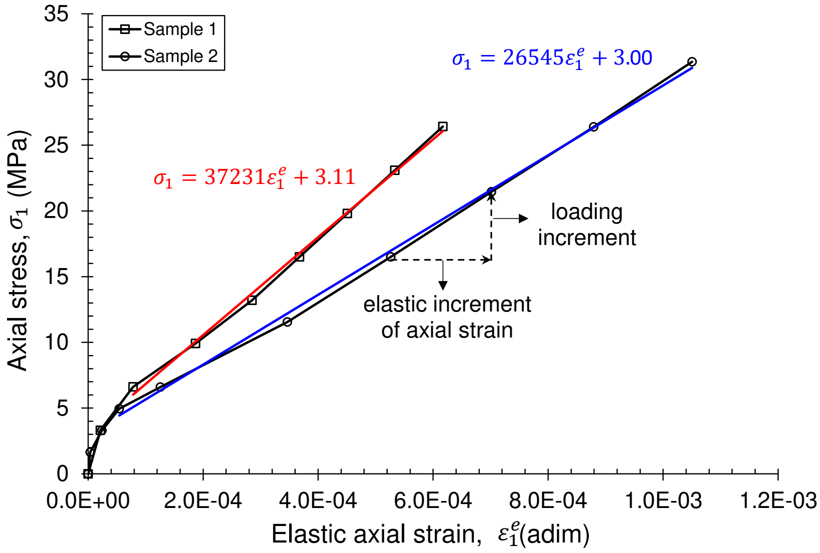

Fig. 4. Axial stress vs elastic axial strain in the laboratory tests.

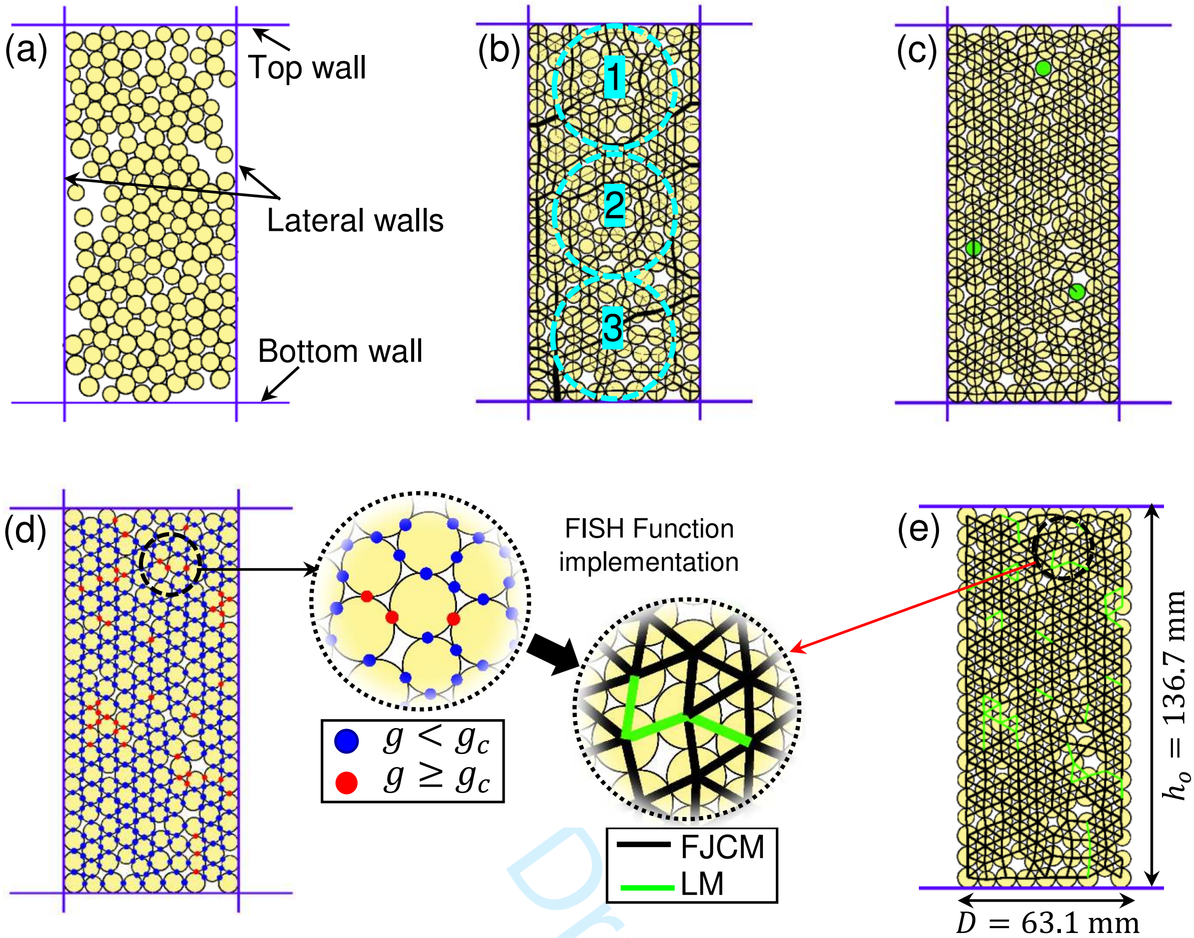

Fig. 5. Genesis of the numerical sample: (a) particle initial generation before rearrangement, (b) contact-force distribution after isotropic stress installation (black lines represent contact-force intensity and cyan lines represent the reference circles to measure stresses), (c) detection of floating particles (green balls represent floating particles), (d) application of the FJCM and LM, (e) final DEM^{2D} specimen (black and green lines represent FJCM and LM network, respectively). Note that to facilitate the visualization, fewer particles are employed herein than in actual simulations (For a color version of this figure refer to the web version of this article) (modified from Gutiérrez-Ch et al. 2018).

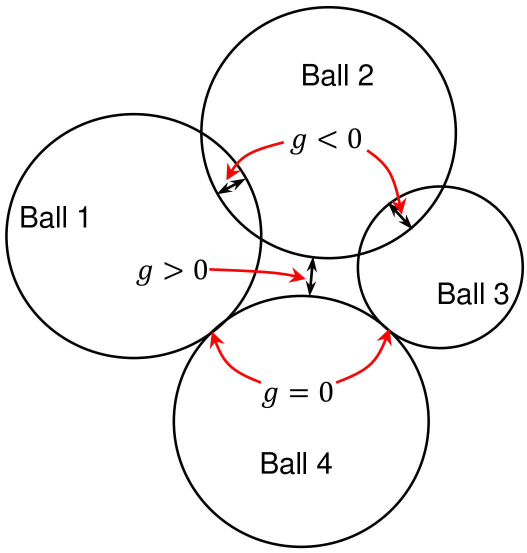

Fig. 6. Idealization of the gap (g) between particles.

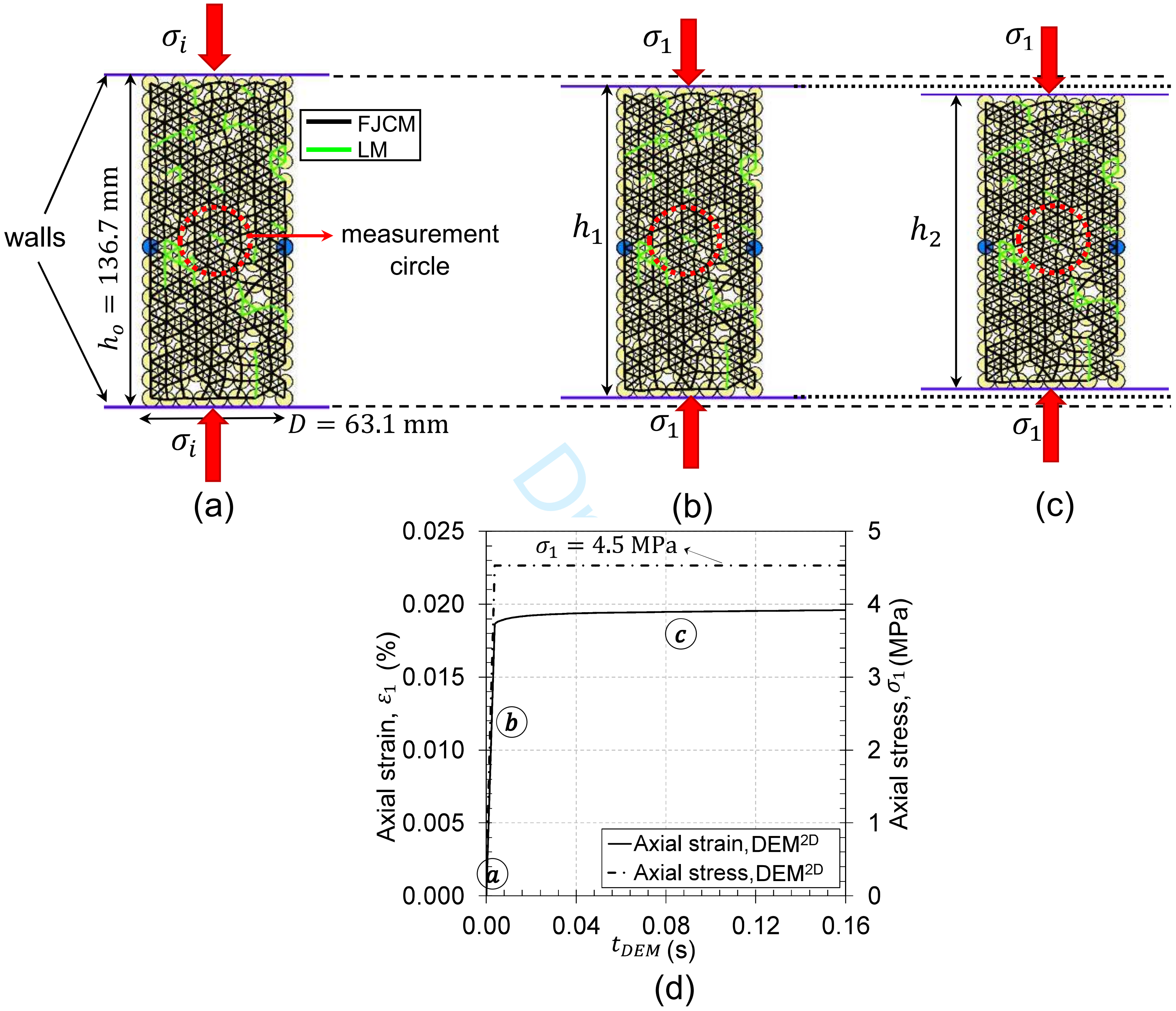

Fig. 7. Numerical uniaxial compression creep test with DEM: (a) initial stress application, (b) compression stage, (c) creep stage (black lines represent FJCM, green lines represent LM, blue balls represent the gage particles), (d) evolution of the axial strain and stress during the test. (For interpretation of the references to color in this figure legend, the reader is referred to the web version of this article).

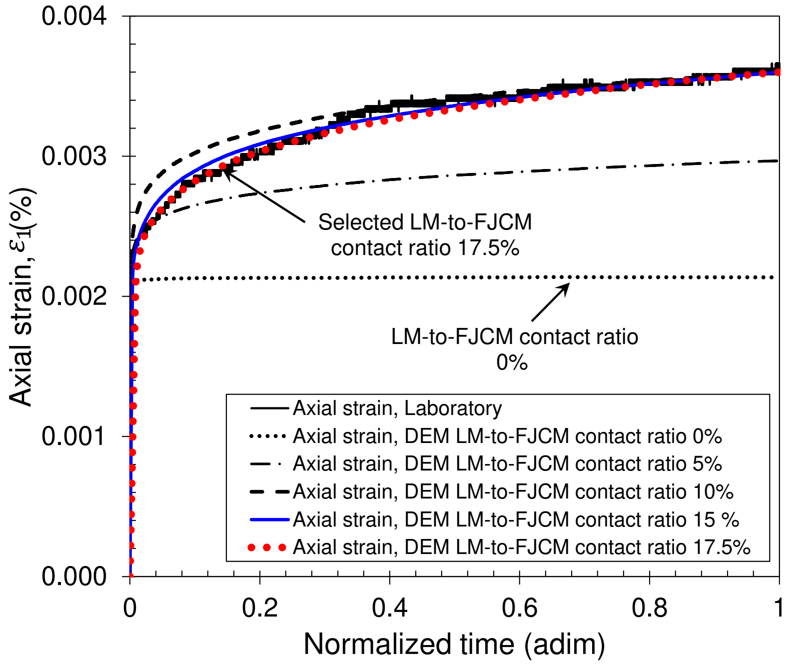

Fig. 8. Sensitivity analysis conducted on Sample 1 to select LM-to-FJCM contact ratio.

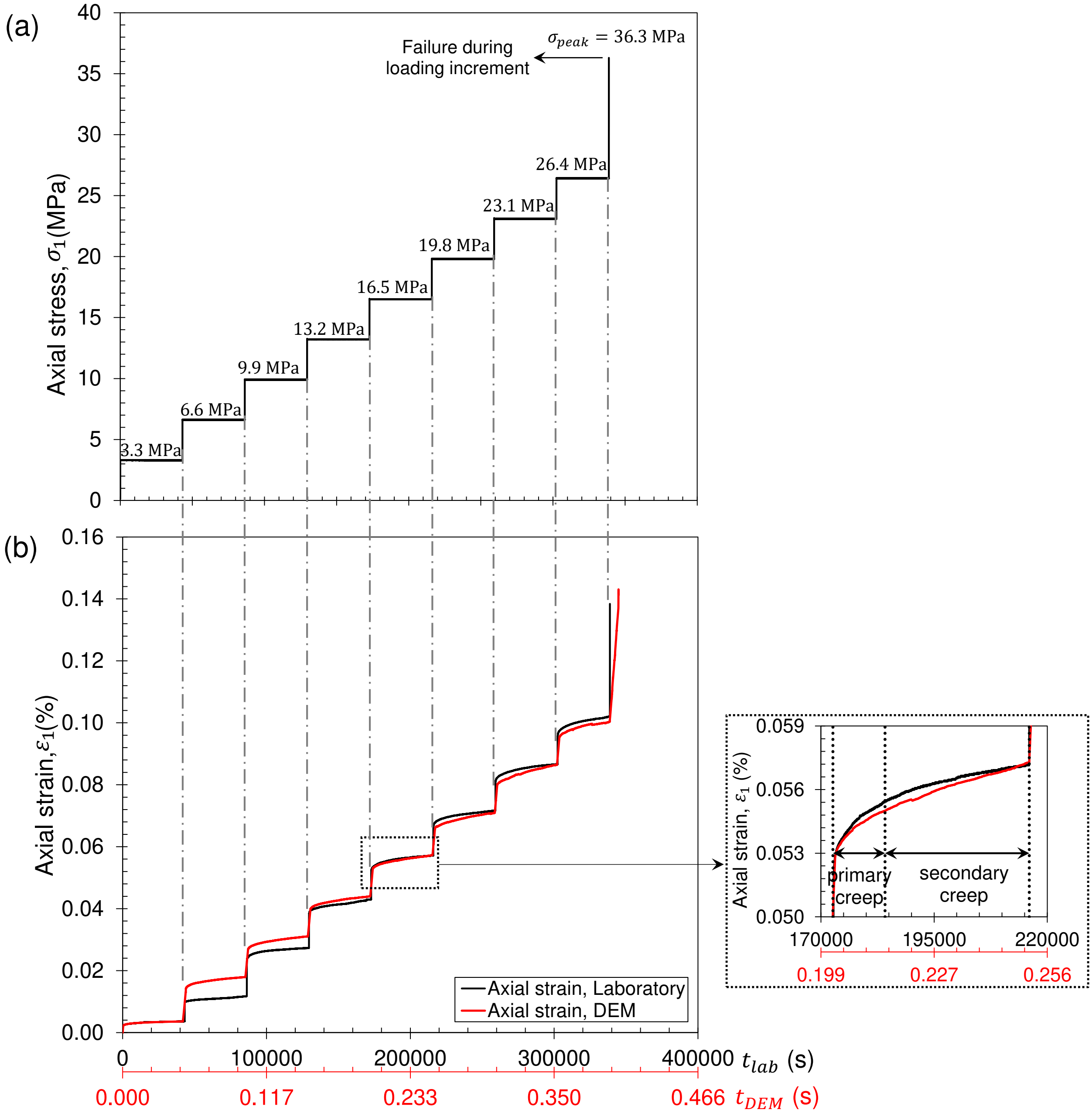

Fig. 9. Comparison between DEM and laboratory results on Sample 1: (a) axial stress (σ_1) vs laboratory time (t_{lab}), (b) creep axial strain (ε_1) vs laboratory time (t_{lab}) and DEM time (t_{DEM}).

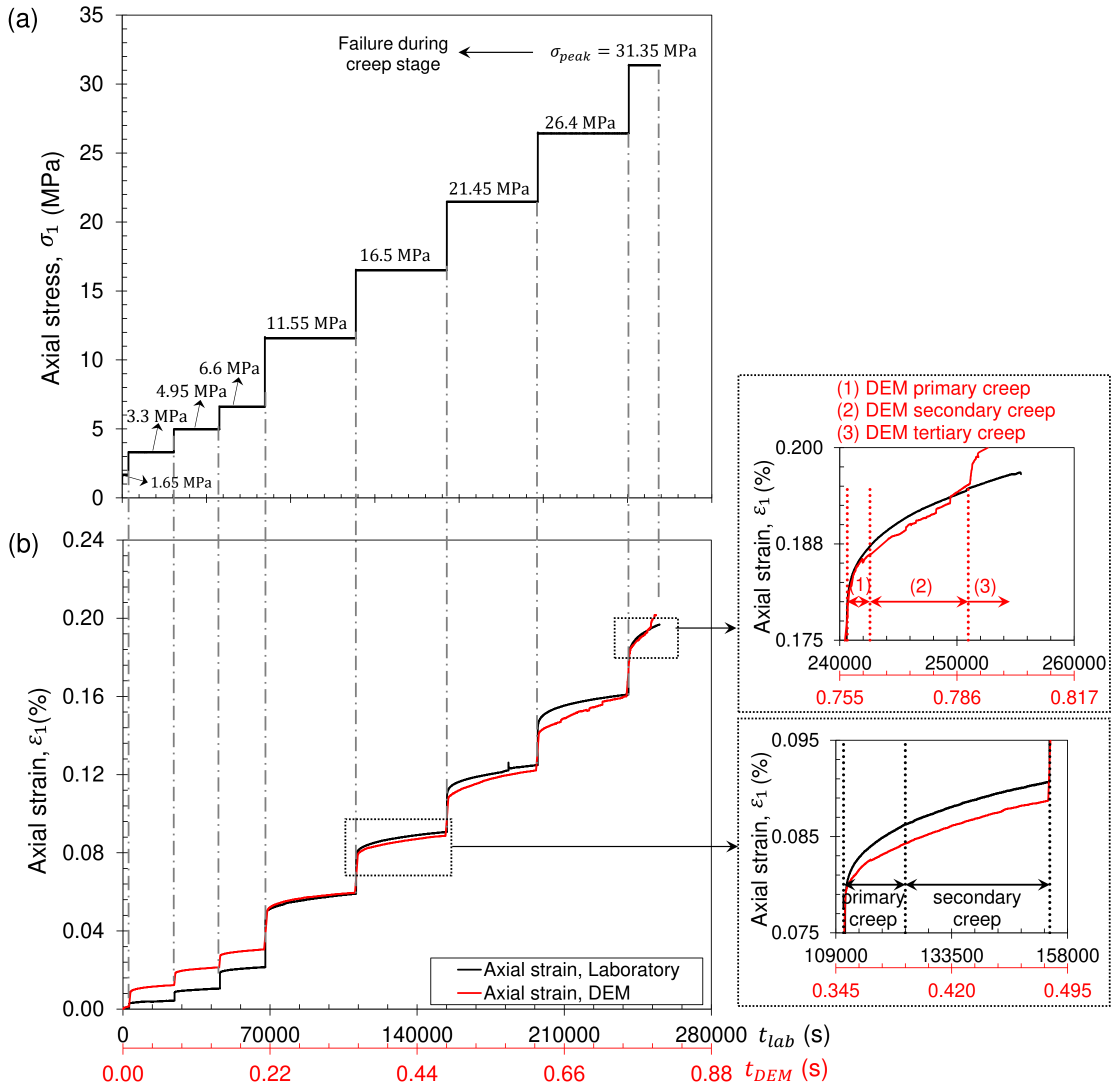

Fig. 10. Comparison between DEM and laboratory results on Sample 2: (a) axial stress (σ_1) vs laboratory time (t_{lab}), (b) creep axial strain (ε_1) vs laboratory time (t_{lab}) and DEM time (t_{DEM}).

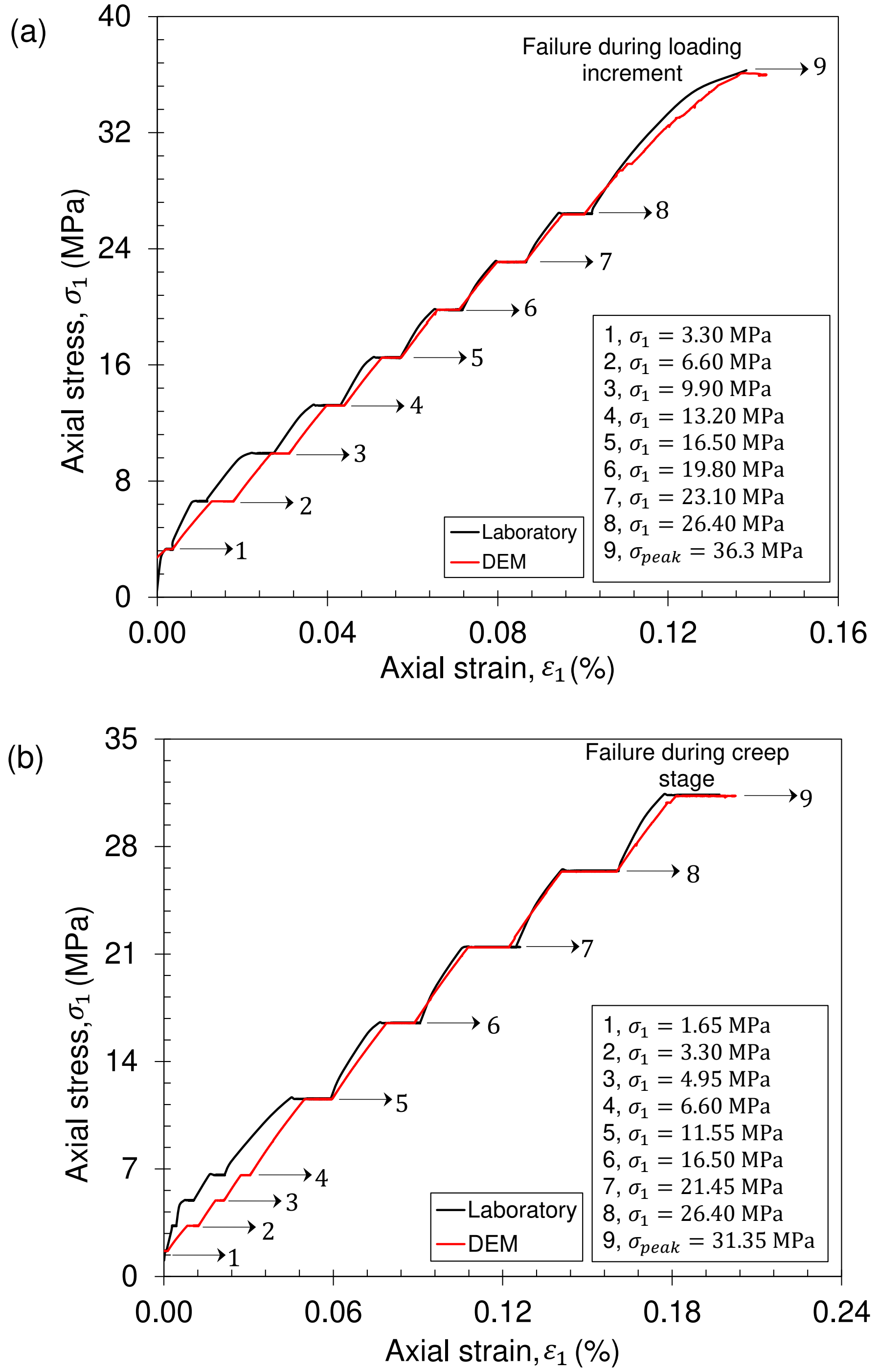

Fig. 11. Comparison between DEM and laboratory axial stress (σ_1) against axial strain (ε_1) during the UCMCT on: (a) Sample 1, (b) Sample 2.

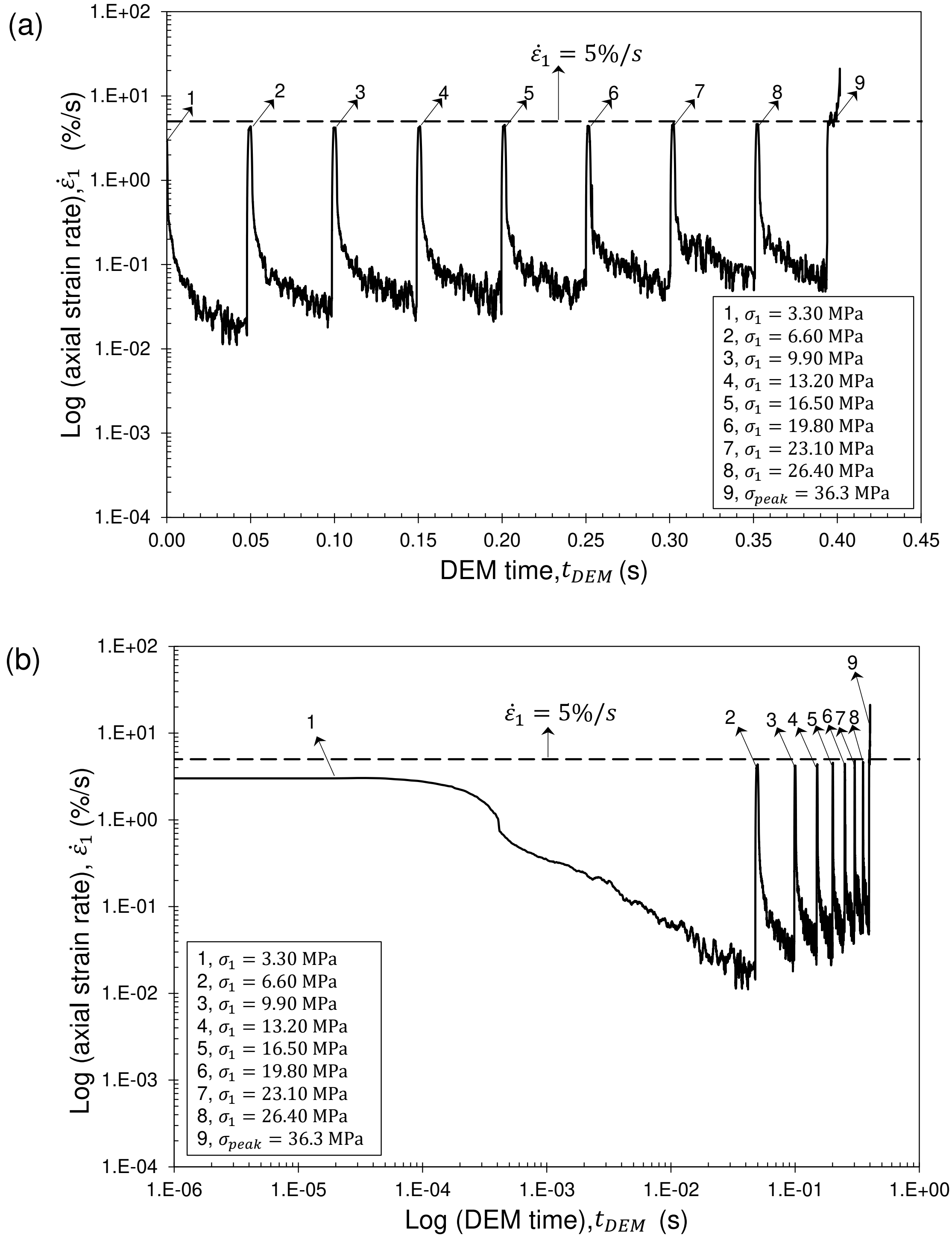

Fig. 12. Axial strain rate ($\dot{\varepsilon}_1$) curve computed with DEM[2D] during the uniaxial compression multistage creep test on Sample 1: (a) log(axial strain rate) vs DEM time, (b) log(axial strain rate) vs log(DEM time).

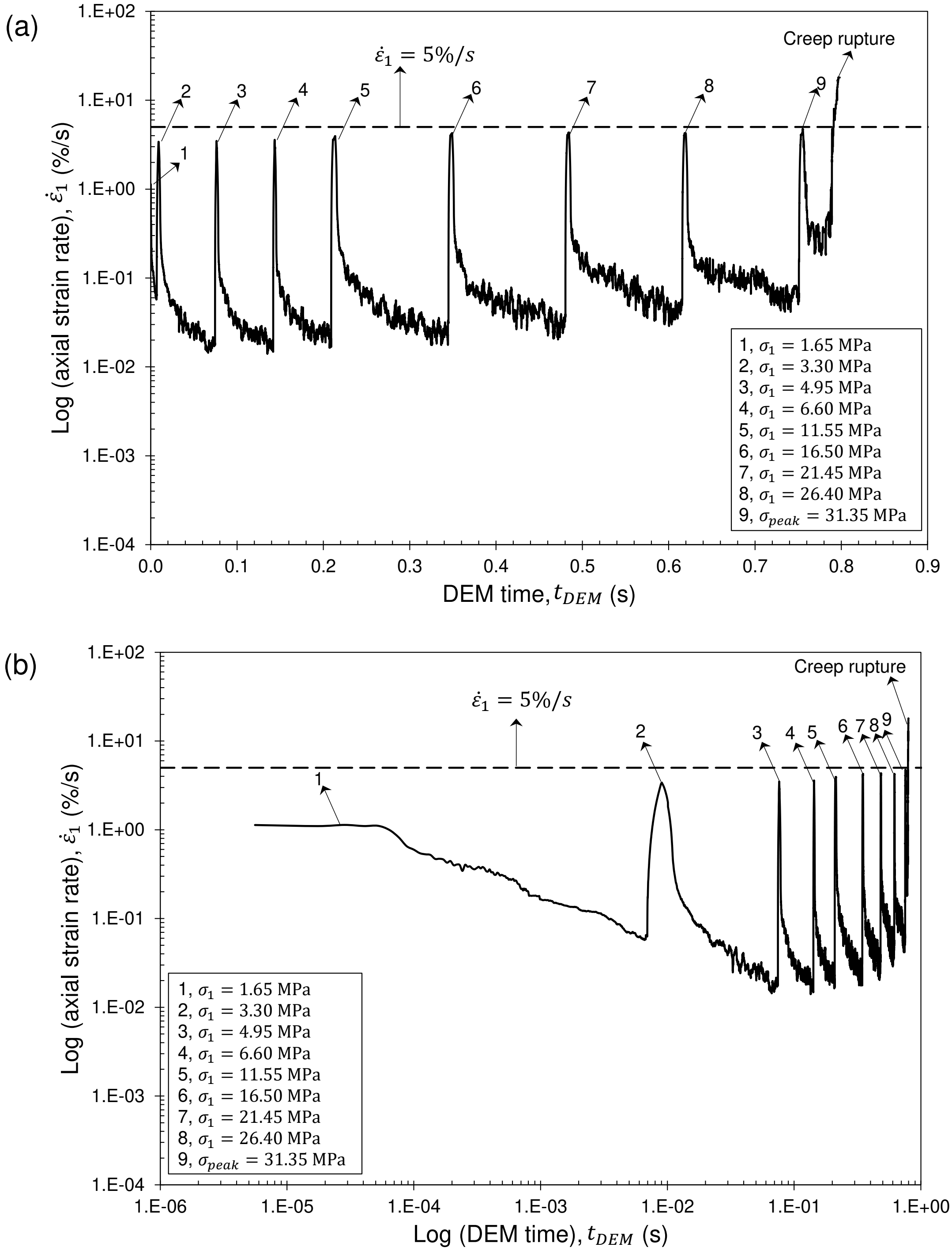

Fig. 13. Axial strain rate ($\dot{\varepsilon}_1$) curve computed with DEM^{2D} during the uniaxial compression multistage creep test on Sample 2: (a) log(axial strain rate) vs DEM time, (b) log(axial strain rate) vs log(DEM time).

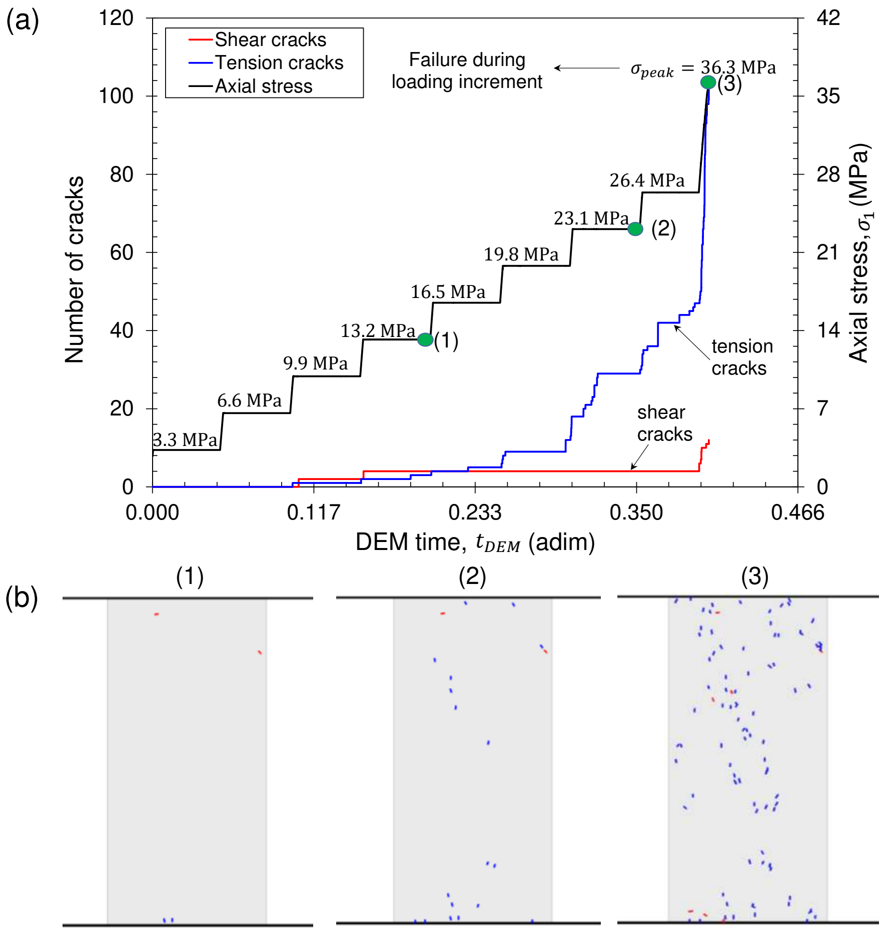

Fig.14. Sample 1: (a) number of cracks developed during the creep tests, plotted against the DEM time (t_{DEM}) computed with DEM[2D]; (b) progressive failure (For interpretation of the references to color in this figure legend, the reader is referred to the web version of this article)

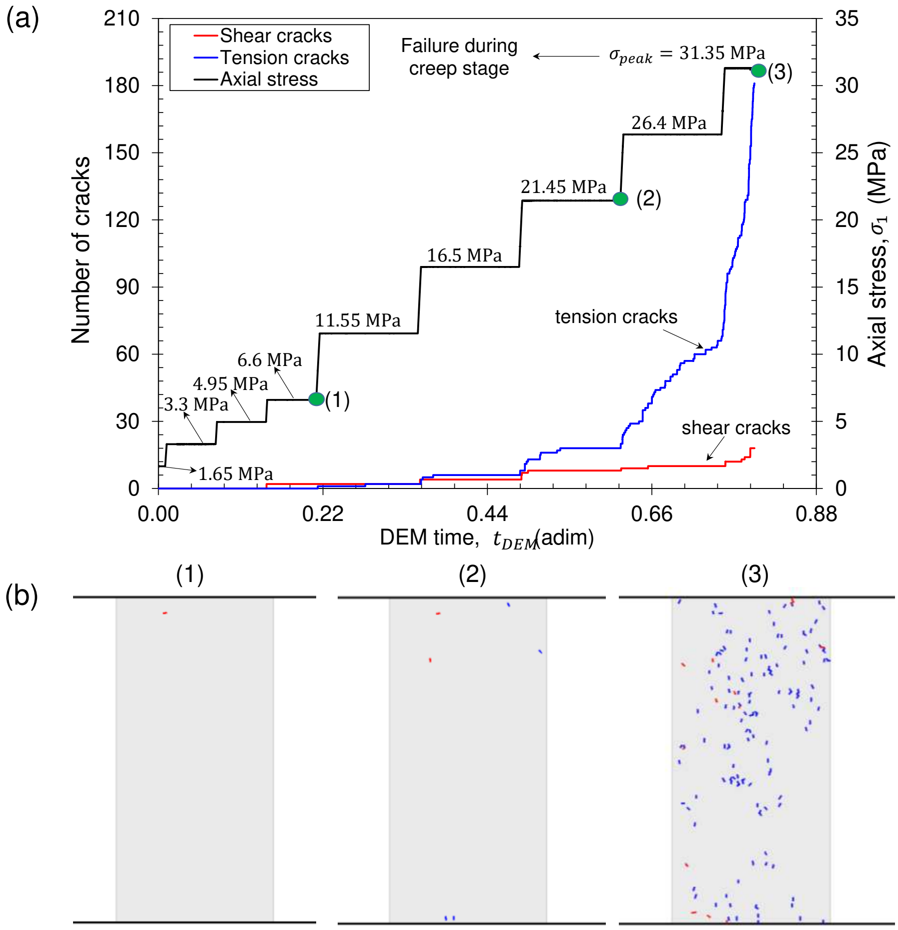

Fig.15. Sample 2: (a) number of cracks developed during the creep tests, plotted against the DEM time (t_{DEM}) computed with DEM^{2D}; (b) progressive failure (For interpretation of the references to color in this figure legend, the reader is referred to the web version of this article)